RSC Advances

ROYAL SOCIETY OF CHEMISTRY

www.rsc.org/advances

ARTICLE TYPE www. rsc.org/xxxxxx | XXXXXXXX

Two-dimensional Germanane and Germanane Ribbons: Density Functional Calculation of Structural, Electronic, Optical and Transport Properties and the Role of Defects†

Jun Zhao,[a,c] **Hui Zeng,**[b,c‡]

Received Xth XXXXXXXXXX 20XX, Accepted Xth XXXXXXXXX 20XX
First published on the web Xth XXXXXXXXXX 200X
DOI: 10.1039/b000000x

We have performed first principles calculations combined with non-equilibrium Green's function to study the structural, electronic, optical and transport properties of two-dimensional germanane and germanane ribbons. More importantly, the defect influences on the properties of the germanane-based nanostructures have been investigated. The presence of single hydrogen vacancy induces ferromagnetism to the nonmagnetic pristine germanane according to spontaneous magnetization, while the formation of the dumbbell structure induced by Ge adatom only reduces the electronic band gap. Both H-monovacancy and dumbbell contained defective germanane nanostructures are thermally stable at room temperature. The optical property calculations revealed that the pristine germanane sheet has significant light absorption of solar spectrum, and the presences of the H-monovacancy and the dumbbell defects in the germanane lead to redshift and blueshift of the light adsorption peak, respectively. Moreover, both zigzag- and armchair-germanane nanoribbons (zGeNRs and aGeNRs) are nonmagnetic semiconductors with direct band gap at the Γ-point, and their band gaps are monotonously reduced with width increasing. Our quantum transport calculations have shown different transport behaviors that depending on the GeNRs' edge topology. While the aGeNRs attain magnetic moment by introducing H monovacancy, it is unlikely to achieve large magnetic moments in germanane via controlling the shape of H-vacancy cluster since the dehydrogenated nanostructures prefer nonmagnetic characteristics after atomic reconstruction. These calculated results suggest that the germanane has not only suitable transmission gap and light adsorption, but also directionally dependent electron transport, making it an excellent candidate for potential applications in the fields of nanoelectronics and optoelectronics.

1 Introduction

Graphene, as the truly two dimensional (2D) crystal successfully exfoliated in 2004, has attracted tremendous interests owing to its unique properties and a broad range of applications in various fields[1]. The creation of graphene has led to the discovery of new and extraordinary electronic transport properties that are lacking in its parent 3D structure[2]. Graphene is envisioned to be the foundation of next generation devices, while the absence of bandgap and the chemical inertness nature of graphene have being widely regarded as obstacles to the application of graphene for nanoelectronics[3]. Nevertheless, the rise of graphene has sparked intense research interests in the fabrication and application of other 2D nanomaterials beyond graphene over the last decade[4]. Correspondingly, more and more fewer- or mono-layered 2D manomaterials, such as hexagonal boron nitride (*h*-BN)[5], topological insulators (mainly including Bi_2Se_3 and Bi_2Te_3)[6], and transition-metal dichalcogenides (TMD) (mainly including MoS_2, WS_2, $MoSe_2$, WSe_2)[7], have been synthesized by mechanical exfoliation or chemical synthesis and are being investigated[8]. Although the 2D nanomaterials like TMDs generally have desirable electronic bandgaps, the carrier mobility is also dramatically decreased compared to the graphene[9]. Improving the electron mobility of the TMDs thus remains a great challenge for their practical applications in nanoelectronics.

Inspired by the intriguing properties of carbon-based 2D materials, graphene- and graphane-like group IV (silicon, germanium, and tin) analogues have been theoretically investigated[10–15]. Among them, monolayer-silicene can only be experimentally prepared on ordered conductor substrate in an ultra-high vacuum to date[16–19], and few layered-germanene and -stanene have also been fabricated very recently by molecular

[a] *School of Chemistry and Chemical Engineering, Collaborative Innovation Center of Advanced Microstructures, Nanjing University, Nanjing 210093, China.*
[b] *School of Physics, National Laboratory of Solid State Microstructures, Nanjing University, Nanjing 210093, China.*
[c] *School of Physics and Optoelectronic Engineering, Yangtze University, Jingzhou 434023, Hubei, China.*
† Electronic Supplementary Information (ESI) available: [details of any supplementary information available should be included here]. See DOI: 10.1039/b000000x/
‡ Corresponding author. E-mail address: zenghui@yangtzeu.edu.cn

beam epitaxy[20,21]. More recently, a free-standing monolayer of hydrogenated puckered germanium (GeH), named as germanane, has been chemically synthesized and experimentally characterized at room temperature[22]. It is unveiled that the monolayer germanane could offer not only sufficient large direct band gap for on/off switching, but also high electron mobility that is crucial for device performance[23,24]. In addition, it has been shown the possibility of tailoring the electronic structure, stability, optical and transport properties of Ge-based 2D nanomaterials via covalent chemistry in terms of attaching different surface ligands[25–27], such as replacing hydrogen saturation with methyl to form $GeCH_3$, leading to substantial improvement in thermal stability[28]. These Ge-based monolayer nanostructures can be chemically synthesized or fabricated by beam epitaxy growth in large quantities for practical applications[29,30]. To date, however, most theoretical calculations have been devoted to accurately compute the electronic band structure of the pristine germanane[11,12,31–34]. The investigations on the the optical and transport properties, and the influences of defects of the germanane-based nanomaterials are still rare[35–37]. In analogy to the case of graphane, the presence of hydrogen vacancies in the 2D germanane is expected to induce magnetization by unbinding the dangling p_z orbital[38]. Recent advances in graphane and silicane have motivated us that cutting the 2D materials into narrowed ribbon could modulate the electronic structure, electronic transport, optical and magnetic properties of zigzag- and armchair-germanane nanoribbons (zGeNRs and aGeNRs)[39,40]. Therefore, it is desirable to explore the structural, electronic, optical and transport properties of the monolayer germanane and the germanane ribbons and the role of defects, which is crucial for further developing the fields of nanoelectronics and optoelectronics.

In this article, we have investigated the structural, electronic, optical and transport properties of two-dimensional germanane and germanane ribbons by using first principles calculations. Moreover, the role of the defects on the properties of the germanane-based nanostructures have been explored. It is found that the presence of a single hydrogen vacancy could convert the nonmagnetic (NM) pristine germanane to a ferromagnetic (FM) semiconductor, while the dumbbell nanostructure induced by Ge adatom attains nonmagnetic ordering. Regarding to the thermal stability of the defects, it is found that both H-monovacancy and dumbbell contained defective germanane nanostructures are stable at room temperature. The pristine germanane has remarkable light absorption of solar spectrum. The presences of the H-monovacancy and the dumbbell defects in the germanane induce redshift and blueshift of the light adsorption peak, respectively. Both zGeNR and aGeNR are nonmagnetic semiconductors, and the electron transport in zGeNRs priors to the aGeNRs due to different trends in their effective electron mass. The aGeNRs attain magnetic moment by means of creating H monovacancy at their surfaces. However, for the $\triangle$-type vacancy conformation, it is a nonmagnetic semiconductor deriving from the extensive reconstruction in the atomic structures. The advantageous features of the germanane-based nanomaterials make them to be promising candidates for potential applications in nanoelectronic and optoelectronic devices.

2 Computational Method

We have perform first-principles calculations within density functional theory utilized in the Vienna *ab initio* Simulation Package (VASP)[41]. The electronic exchange-correlation potential was described within the generalized gradient approximation (GGA) in the form of Perdew-Burke-Ernzerhof (PBE)[42]. The electronic wave functions were expanded using projector augmented wave (PAW) method with a cutoff energy of $500eV$. The primitive cell of germanane sheet was fully relaxed in terms of both lattice constants and atomic positions until the electronic self-consistent energy was less than $10^{-5}eV$ and the force on each atom was less than $0.03eV/\AA$ by using the conjugate-gradient method. To investigate the influences of isolated single hydrogen vacancy defect and Ge adatom dopant, a sufficient large supercell should be considered in the computation because defect-defect coupling can be pronounced in a small supercell. For this purpose, we thus consider a 4×4 supercell to minimize the defect-defect interactions. In general, the localized state arising from the vacancy or adatom defect emerges as a flat band in the electronic band structure. The supercell was imposed to periodic boundary condition (PBC), and in the direction perpendicular to the sheets we used a lattice parameter of $20\AA$, which was sufficient to prevent image interactions. For the electronic structure calculations, the Brillouin zone is sampled with $21\times21\times1$ for the 2D germanane and $1\times25\times1$ for the GeNRs, in the Monkhorst-Pack k mesh scheme[43]. A one-dimensional PBC was applied along the ribbon's length direction. The vacuum distance between the ribbon edges is $15\AA$.

To simulate the transport properties, a two-probe computational approach implemented in the Nanodcal code is employed[44,45]. The theoretical model is built in such a way that the central region consisting of an optimized supercell, which is surrounded by two semi-infinite leads made of pristine primitive cell on each side. We use the numerical double ζ plus polarization (DZP) basis set and $3000eV$ as mesh cutoff for all atoms in the quantum transport calculations. The interaction between the valence electrons and the atomic core is computed within the standard norm-conserving Troullier-Martins pseudopotential[46]. The quantum conductance (G) and the transmission coefficient (T) as a function of electron energy is calculated in the framework of Laudauer-Büttiker formalism[47]. The current driven by an external bias voltage is

computed from the transmission coefficient. Moreover, the detailed methodology and practical implementation of the non-equilibrium Green's function approach (NEGF) is available in Ref.[48]. Moreover, the drawings were produced by the visualization software VESTA[49].

3 Results and Discussion

3.1 Two-dimensional Germanane Sheet

For a better understanding of defective 2D germanane and GeNRs, we firstly start with the pristine 2D germanane that is derived from the hydrogenation of germanene, where each Ge atom is saturated by one hydrogen atom, as shown in Figure 1. Previous studies have found that the chair-like configuration of infinite sheet of 2D germanane is energetically more favorable than the boat-like configuration[15,31]. In the germanane crystal, each Ge atom is bound to three three adjacent Ge atoms and one hydrogen atom to form the puckered nanostructure due to the sp^3-like hybridization, exhibiting the angle of θ_{Ge} and θ_H of 110.70° and 107.25°. The perpendicular distance between A- and B-sublattices of the Ge atoms is approximately 0.73Å, which is larger than the buckling distance of germanene[10]. Correspondingly, the calculated lattice constant of the germanane is increased to 4.09Å, which is in good agreement with previously reported survey[11,12,31–33,50]. Hence, the bond lengths of the Ge-Ge bond and Ge-H bond stretch to 2.473Å and 1.563Å, respectively. The cohesive energy E_{coh} of the 2D germanane sheet (per unit cell) relative to free Ge and H atoms is calculated by equation:

$$E_{coh} = 2 \times E_T^H + 2 \times E_T^{Ge} - E_T^{Germ} \quad (1)$$

where E_T^H (E_T^{Ge}) is the total energy of single free H (Ge) atom, and E_T^{Germ} is the total energy of germanane. The calculated cohesive energy per unit cell of germanane is $11.53eV$, indicating that the formation of germanane is energetically more favorable than the graphane[39]. Due to the sp^3-like hybridization for all Ge atoms, germanane is a nonmagnetic (N-M) semiconductor with a direct band gap of $0.95eV$, as shown in the Figure 1. It is well known that GGA-PBE within DFT framework would underestimate band gap. More accurate calculations, generally approached by Heyd-Scuseria-Ernzerhof (HSE) hybrid density functionals including screened Coulomb potential and GW corrections, have reported a band gap of $1.5eV$ and even larger value for the monolayered germanane[33]. Both the valence band maximum (VBM) and conduction band minimum (CBM) of the germanane are located at the Γ point. As shown in the projected density of states (PDOS), the VBM is derived from Ge $4p$ orbitals, and the CBM is composed by the Ge-Ge antibonding state. The VBM of the germanane are double degenerate at Γ-point in the exclusion of spin-orbit coupling (SOC), and it is attributed to the Ge-Ge bonding state of p_x and p_y orbitals. These two degenerate bands are splitting by $0.2eV$ with the inclusion of SOC. Additionally, Li *et al* have reported that the band gap of the germanane monolayer can be reduced to zero when a biaxial tensile strain is applied[51]. The main focus of this work is the spin-polarized electronic structures influenced by defects and the transport properties. To eliminate the long range effects induced by point defects, a large supercell is essential in calculations. The calculations based on HSE functional are extremely time-consuming and only practically implemented in a small supercell. Correspondingly, we have performed the spin-dependent computations by using PBE functional.

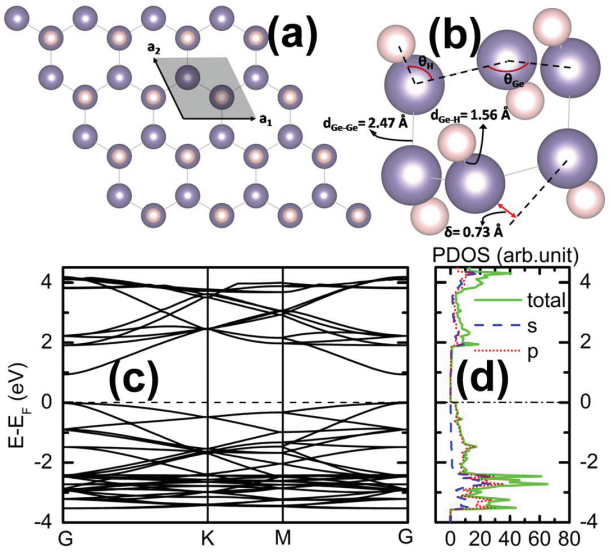

Fig. 1 (Color Online) (a) Top (left panel) and (b) perspective (right panel) view of the atomic structure of the 2D germanane sheet with buckled honeycomb structure. Purple (dark) and whit (light) balls represent germanium and hydrogen atoms, respectively. The primitive cell with Bravais lattice is denoted by vectors $\vec{a}_1$ and $\vec{a}_2$, and the buckling of Ge plane is denoted by δ. The θ_{Ge} and the θ_H are the Ge-Ge-Ge and Ge-Ge-H bond angles in germanane, respectively. Relevant structural parameters are summarized in Table 1. (c) Electronic band structure and (d) projected density of states (PDOS) of the pristine germanane sheet.

3.2 Defect in Germanane Sheet

The hydrogen vacancy and adatom in the Si- and Ge-based nanostructures could induce magnetization as a result of the presence of unpaired orbitals by changing the sp^3-like to the sp^2-like hybrid orbital[33,52,53]. We thus investigate the effects of single H vacancy and Ge adatom in the 2D germanane sheet, as shown in Figure 2. The presence of the hydrogen monovacancy has no significant effects on the atomic nanostructure, leading to the transformation of sp^3 bonding into sp^2

bonding for the dehydrogenated Ge atom. We have carried out nonlinear magnetic calculation and identified the emergence of permanent magnetic moment $\sim 1\mu_B$ at the Ge atom because one electron accommodated by the dangling p_z orbital becomes unpaired, which is in good agreement with previously reported simulations[53]. To assess the stability of the defected nanostructure, we have calculated the formation energy in term of $E_{for} = E_T^{defect} - n_{Ge} \times E_T^{Ge} + n_H \times E_T^H - E_T^{Germ}$, where E_T^{defect} (E_T^{Germ}) is the total energy of the defected (pristine) germanane sheet, and n_{Ge} (n_H) is the number of H vacancy (Ge adatom) atoms, and E_T^H (E_T^{Ge}) is the total energy of single free H (Ge) atom. The calculated results revealed that the dehydrogenation of a single H atom on germanane sheet is endothermic with formation energy of $3.55eV$ in a 4×4 supercell. Generally, the dehydrogenation in the germanane sheet causes negligible changes in the electronic band structure, as shown in Figure 3. However, the opposite spin states are significantly polarized around the Fermi level. Both the VBM (denoted as α) and the CBM (denoted as $\alpha\prime$) are located at the Γ point, leading to a direct bandgap of $0.81eV$. Detailed analysis demonstrated that both α- and $\alpha\prime$-subbands are originated from exchange splitting of the degenerate bands. Moreover, the isosurface charge densities (shown in Figure 3c and Figure 3d) generating the flat bands below and above the Fermi level for the up- and down-spin components are substantially localized at the vacancy defect with minor contributions from adjacent Ge atoms. The flat defect bands lead to very narrow PDOS peaks around the Fermi level, as shown in Figure 4a, suggesting that the magnetic moment of $1\mu_B$ per H vacancy is governed by Stoner ferromagnetism[54]. Both VBM and CBM are contributed mainly by Ge $4p$ orbitals ($\sim 70\%$) and secondarily by Ge $4s$ orbitals ($\sim 20\%$), and the contribution of the H atoms can be neglected. Hence, it is rather intriguing to tune the electronic bandgap and magnetic properties of germanane sheet by dehydrogenation.

For Ge adatom case, in analogy to the adsorption of a single Si adatom on silicene sheet[55], the Ge adatom prefers the top (T) site and presses down the bottom (B) Ge atom to form a dumbbell structure, as shown in Figure 2. The two Ge atoms positioned at two ends of the dumbbell are denoted as T and B. The distance between the T(B) Ge atom and the nearest Ge atoms (marked A, C, and D) is 2.55Å, which is slight larger than the Ge-Ge bond length in the pristine germanane. Hence, the depletion of electric charge of the T(B) atom is ~ 0.2 electron, which is transferred to the nearest three Ge atoms. The second-nearest six Ge atoms also experience substantial change. It is noticed that the four H atoms that originally bonded with the four Ge atoms (marked A-D) in the pristine germanane are desorbed. The Ge-Ge bond of the T-B site is relatively weak and the bond length is 2.94Å. Moreover, each T(B) site Ge adatom forms three Ge-Ge bonds with bond angles of 91.2°, which is closer to the tetrahedron angle

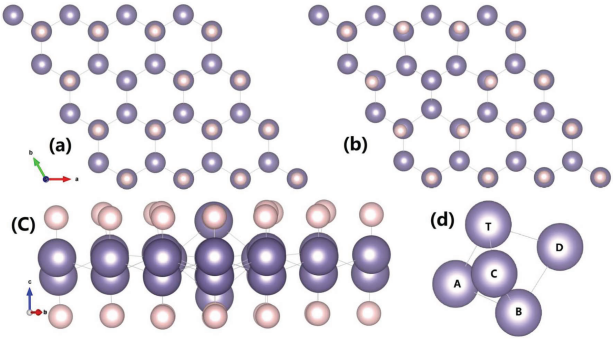

Fig. 2 (Color Online) Atomic structures of the defected germanane consisting of (a) H monovacancy and (b) Ge adatom. Purple (dark) and white (light) balls represent germanium and hydrogen atoms, respectively. (a) Top view of the atomic structure of the H monovacancy configuration. (b) Top view and (c) side view of the atomic structure of the Ge adatom configuration that forming dumbbell-like nanostructure. (d) Zoomed dumbbell nanostructure, T (B) denote the Ge atoms at the top (bottom) site of the dumbbell, and A, C, and D are the Ge atoms nearest to the T and B sites.

of the diamond. The dumbbell structure has formation energy of $E_{for} = 6.35eV$ for single Ge adatom in the 4×4 supercell because it referred to the dehydrogenation of four H atoms. In addition, the isosurface charge densities shown in Figure 3e revealed that the VBM is derived from the bonding state. The CBM is composed by the antibonding state with rather uniform distribution at every Ge atom. It is reported that such dumbbell structure in silicene could induce spin-polarized ground state and a small band gap opening ($\sim 0.09eV$)[56]. However, the dumbbell structure in germanane is predicated to be nonmagnetic semiconductor with a direct band gap of $0.79eV$*. This is attributed to the suppression of spontaneous ferromagnetism transition, because the exchange energy due to spin polarization is smaller than the cost in band energy according to Stoner criterion[57]. As a result, the dumbbell structure attains nonmagnetic properties and the magnetic moment in the supercell is zero, which is also confirmed by the degenerated PDOS shown in Figure 4b. In addition, it is noticed that the adsorption of Ge adatom is rather different from the adsorption of metal atom on the surface of germanene surface, which is due to the semi-metallic character deriving from the mixed sp^2-sp^3 hybridization in the germanene sheet[58]. The introducing of dumbbell structure in the germanane sheet only reduces the electronic band gap due to the atomic reconstruction around the Ge adatom.

The average equilibrium concentration of defects at finite

* We also have set parallel and antiparallel spin moments for these off-plane Ge atoms, but their spin moments spontaneously decreased to zero after spin-polarized DFT calculations. The nonlinear magnetic calculations also conducted the same results.

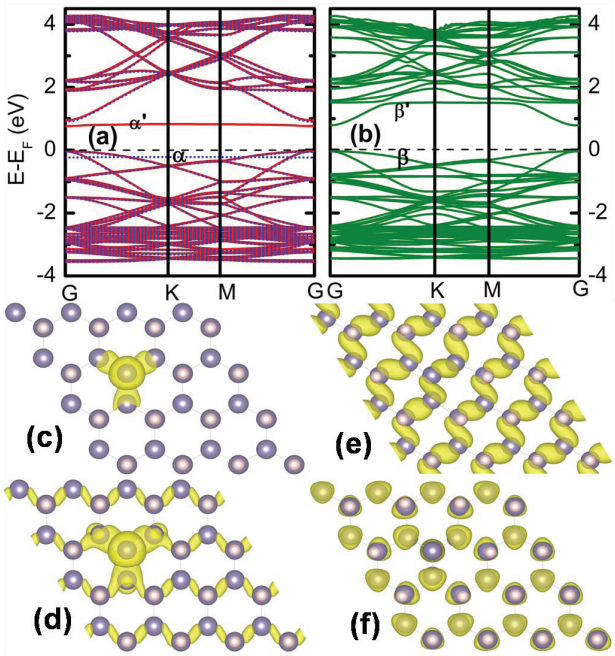

Fig. 3 (Color Online) Electronic band structure of the defected germanane consisting of (a) single H vacancy and (b) Ge adatom. (a) Spin-polarized structure with dotted blue and solid red lines representing the up-spin and the down-spin states, respectively; the VBM- and the CBM-subbands are denoted by α and $\alpha\prime$, respectively. (b) Spin-unpolarized band structure; the VBM- and the CBM-subbands are denoted by β and $\beta\prime$, respectively. (c)-(d) The isosurface charge densities corresponding to the α and $\alpha\prime$ subbands, respectively. (e)-(f) The isosurface charge densities corresponding to the β and $\beta\prime$ subbands, respectively.

temperature T can be assessed by[54]:

$$n/N = exp(-E_{for}/k_BT) \quad (2)$$

where n (N) is the number of the defect (total) atoms in the germanane nanosheet, and E_{for} is the formation energy and k_B is the Boltzmann's constant. At room temperature, Eq.2 yields a very low defect concentration, which can be used to understand Bianco's experimental observation and thus large scale defect-free germanane sheet is successfully fabricated[22]. Based on the total energy calculations, the H monovacancy and Ge adatom nanostructures discussed above are determined to be stable. However, considering thermal stability, these defective nanostructures may not be stable at high temperature. To address the issue of the temperature effect, we further have performed *ab initio* molecular dynamics (MD) simulation at room temperature for these defective nanostructures, as shown in the Electronic Supplementary Information. The MD simulation confirms that both H monovacancy and Ge adatom contained nanostructures are thermally stable at room temperature.

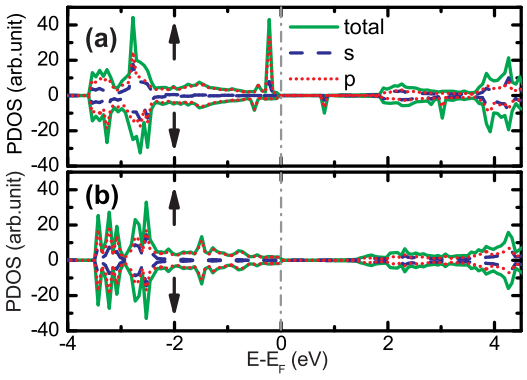

Fig. 4 (Color Online) Projected density of states of the defected germanane consisting of (a) single H vacancy and (b) Ge adatom. The up- and the down-arrows denote the up- and down-spin states, respectively. The solid green, dashed blue and dotted red lines representing total, s-orbital and p-orbital contribution to the density of states.

3.3 Optical Properties

Previous studies have demonstrated that 2D germanane nanomaterial is rather attractive for efficient light harvesting and has promising applications in optoelectronics[22]. We thus investigate the optical properties based on *ab initio* calculations of dielectric function[59]. The optical properties of the 2D nanomaterials are determined by the in-plane dielectric function for normal incidence. The imaginary part $\varepsilon_2(\omega)$ of the dielectric function is calculated by a summation of optical transition matrix element over empty states:

$$\varepsilon_2(\omega) = \frac{4\pi^2e^2}{\Omega}\lim_{q\to 0}\frac{1}{q^2}\Sigma_{C,V,K}2W_K\delta(\varepsilon_{CK}-\varepsilon_{VK}-\omega) \times \langle u_{CK+e_{\alpha}q}|u_{VK}\rangle\langle u_{CK+e_{\beta}q}|u_{VK}\rangle^* \quad (3)$$

where the indices C and V refer to conduction and valence band states, respectively. The real part $\varepsilon_1(\omega)$ then can be calculated from the obtained imaginary part $\varepsilon_2(\omega)$ through the Kramer-Kroning transformation. Furthermore, the frequency-dependent optical absorbance $A(\omega)$ is computed by:

$$A(\omega) = \sqrt{2}\omega[\sqrt{\varepsilon_1^2(\omega)+\varepsilon_2^2(\omega)}-\varepsilon_1(\omega)]^{\frac{1}{2}} \quad (4)$$

The $\varepsilon_2(\omega)$ for the pristine germanane and the defected germanane nanostructures is plotted in Figure 5. For the pristine germanane sheet, it exhibits photon energy absorption starting at approximately $0.9eV$, which is explicitly demonstrated in the zoomed optical absorbance $A(\omega)$. This is because

the absorption takes place for $\hbar\omega > E_g$. There are two remarkable $\varepsilon_2(\omega)$ peaks at about $1.36eV$ and $3.39eV$, which are corresponding to significant light absorption at infrared and ultraviolet-visible region of solar spectrum. The presences of the H monovacancy and the Ge adatom defects make the absorption starting point moving towards photon energy increasing and reduction, respectively. These calculated absorbance $A(\omega)$ results of the defected nanostructures are consistence with their energy gaps shown in Figure 2. Moreover, the H monovacancy and the Ge adatom defected nanostructures display redshift and blueshift of the light adsorption peak compared to that in the pristine germanene sheet. Specifically, it is interesting to find a absorption peak at $2.42eV$ for the Ge adatom contained defective nanostructure, which is corresponding to substantial visible light absorption. Since the optical properties are sensitive to the structural modifications, e.g. the optical absorbance, it could be used to identify the defects in the germanane based nanomaterials.

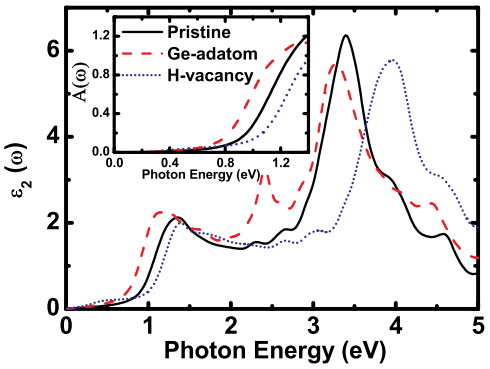

Fig. 5 (Color Online) The calculated imaginary part $\varepsilon_2(\omega)$ of dielectric functions vs photon energy for the pristine 2D germanane (black solid line), the defected germanane containing Ge adatom (red dashed line), and the defected germanene containing H monovacancy (blue dotted line). It is noticed that the light incidence along c direction and the polarization along a/b direction (indicated in Figure 2). The inset shows the infrared optical absorbance vs photon energy.

3.4 Germanane Nanoribbons

The 2D germanane can be tailored into narrowed ribbon structure that could offer tunable band gap for various applications[35]. The germanane nanoribbons (GeNRs) can be classified into zigzag- and armchair-GeNRs according to their edge morphology. Following the previous convention[60], the width of GeNRs are defined by parameter N: for zGeNRs, N denotes the number of zigzag carbon chains along the nanoribbon axis; for aGeNRs, N denotes the number of Ge-Ge dimers in the unit cell that paralleling to the axis of the nanoribbon. The buckling distance (denoted by δ in Figure 1), which is uniformly $0.73\AA$ in the 2D germanane crystal, is unchanged for the inner Ge-Ge bond and increased to $0.78\AA$ for the edge Ge-Ge bond for both zGeNRs and aGeNRs. Figure 6 shows the atomic nanostructures of the particular cases: 6-zGeNR and 11-aGeNR; all Ge atoms are passivated by H atoms to form sp^3 hybridization. We have examined the atomic structures and the electronic properties of N-zGeNR with $N = 4 \sim 10$ (width from $1.468nm$ to $3.594nm$) and N-aGeNRs with $N = 4 \sim 17$ (width from $0.862nm$ to $3.518nm$). More importantly, we have performed both spin-unpolarized and spin-polarized calculations to identify the ground state of GeNRs. Two primitive cell is used as supercell in the calculations to allow possible FM and AFM magnetic configurations along the edge of the GeNRs. It is found that there is no essential difference in total energy between various magnetic configurations taken into account. Therefore, both zGeNRs and aGeNRs have NM ground state.

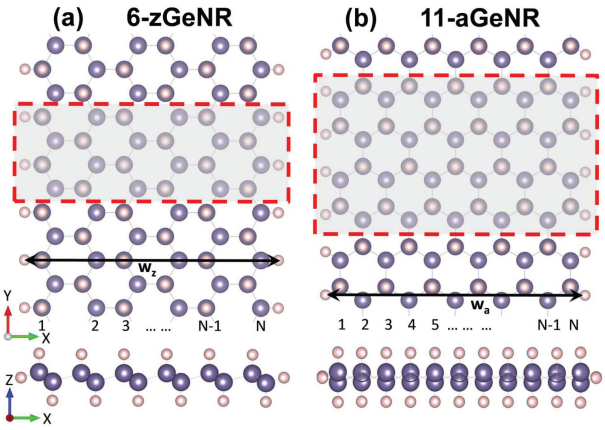

Fig. 6 (Color Online) Atomic structures of the optimized (a) 6-zGeNR and (b) 11-aGeNR with bird-view (top panel) and side-view (bottom panel). All the Ge (purple ball) are saturated by H (white balls). The width of the GeNRs are denoted w_z and w_a for N-zigzag and N-armchair GeNRs, respectively. Double unit cell of the GeNRs is delineated by dashed lines (red color online) with the lattice constant 2a. The electron transport takes place along y direction.

In order to access the stability, we have calculated the zero-temperature edge formation energy per length ε_f in terms of:

$$\varepsilon_f = \frac{1}{2L}[E^{ribbon} - N_{Ge}E^{ger} - \frac{1}{2}(N_H - N_{Ge})E_{H_2}] \qquad (5)$$

where L is the length of the germanane ribbon, and E^{ribbon} and E^{ger} are the total energies of the GeNR supercell and 2D germanane sheet, respectively; N_{Ge} and N_H are the numbers of Ge and H atoms in the GeNR supercell. For the N-zGeNRs, the

edge formation energy is slightly changed from $52.6meV/\AA$ for the 4-zGeNR to $52.7meV/\AA$ for the 10-zGeNR. For the *N*-aGeNRs, the calculated edge formation energy is $59.9meV/\AA$ for the 4-aGeNR, and continually increase to $60.7meV/\AA$ for the 7-aGeNR and remains this value until 17-aGeNR. Apparently, the ε_f is independent on the the ribbon width. To investigate the effect of temperature and gas pressure on the thermodynamic stability of the GeNRs to the 2D germanane sheet, we further have examined the Gibbs free energy (G_{H_2}), which is calculated as a function of chemical potential μ_{H_2} of H_2 molecule according to the following formula[61]:

$$G_{H_2} = \varepsilon_f - \frac{1}{2}\rho_H \mu_{H_2} \quad (6)$$

where $\rho_H = \frac{1}{2L}(N_H - N_{Ge})$ is the edge hydrogen density. We have shown the Gibbs edge free energy for the 6-zGeNR and the 11-aGeNR in Figure 7, where the lowest energy corresponds to the most thermodynamically stable nanostructure. The aGeNR is slightly more stable than zGeNR at high hydrogen concentration. It is noticed that at ambient conditions ($T = 300K$ and partial pressure $p = 5 \times 10^{-7} bar$ that corresponding to $\mu_{H_2} \approx -0.69eV$), the zGeNR is found to be energetically more favorable than the aGeNR. The difference in G_{H_2} between the aGeNRs and zGeNRs is only $21.1meV/\AA$ under ambient conditions. In addition, the 2D germanane sheet is more favorable than the GeNRs except at very high partial pressures of H_2. Our calculated Gibbs free energy is in good agreement with the theoretical investigation for the 7-aGeNR and 4-zGeNR that published recently, and furthermore, it is found that the 2D germanane monolayer could spontaneously assemble into GeNRs when atomic H serves as hydrogen source[62].

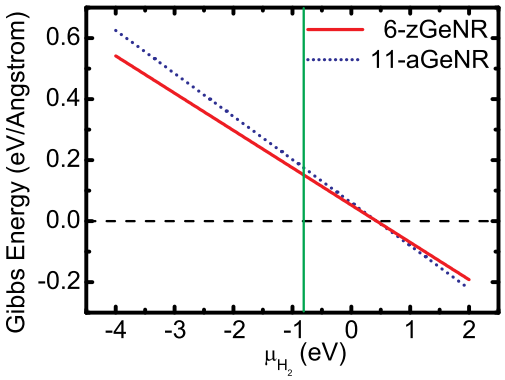

Fig. 7 (Color Online) The Gibbs free energies G_{H_2} as a function of chemical potential of hydrogen gas μ_{H_2} for the 6-zGeNR and 11-aGeNR. The free energy of the 2D germanane, which is indicated by dashed horizontal line at $G_{H_2} = 0$, is also shown for comparison. The vertical green line delineates the ambient condition.

The electronic structures of the 6-zGeNR and 11-aGeNR are presented in Figure 8. Both 6-zGeNR and 11-aGeNR are NM direct band gap semiconductors because all Ge atoms in GeNRs are sp^3 hybridization and thus ensure fourfold coordination for edge atoms. For 6-zGeNR and 11-aGeNR cases, both VBM and CBM are located at the Γ-point, and their band gaps are $1.47eV$ and $1.52eV$, respectively. The analysis of charge density isosurfaces of the VBM- and CBM-subbands revealed that they are delocalized and rather uniformly distributed at Ge atoms throughout the GeNRs.

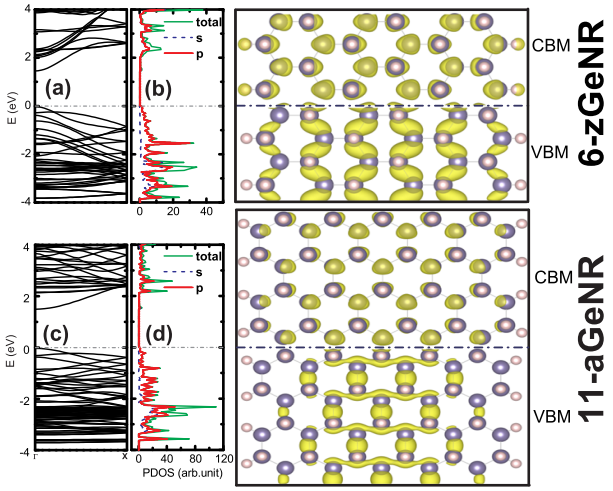

Fig. 8 (Color Online) (a) Electronic band structure and (b) projected density of states (PDOS) of the 6-zGeNR, and the corresponding charge densities of CBM-subband (top) and VBM-subband (bottom) are shown in the righthand panel. (c) Electronic band structure and (d) projected density of states (PDOS) of the 11-aGeNR, and the corresponding charge densities of CBM-subband (top) and VBM-subband (bottom) are shown in the righthand panel. The Fermi level is set to zero, which is also shown by dashed-dotted (light gray online) line.

It is well known that the band gap of the graphene nanoribbons is dependent on their width and edge state. The armchair graphene nanoribbons are found to have an aromatic dependence of their band gaps with the width defined by *N*, and such aromaticity is absent in graphane nanoribbons[39,60]. It is interesting to examine the band gap variations as a function of GeNRs' width for both zGeNRs and aGeNRs, and relevant results are shown in Figure 9a. Both zGeNR and aGeNR families display distinct quantum confinement effect, e.g., their band gaps are monotonously reduced with respect to *N* increasing because the quantum confinement becomes weaker, which is very similar to the recent survey[62]. This is attributed to the sp^3 hybridization in the GeNRs that eliminating the resonance states, and thus the band gaps are only governed by the quantum confinement. Similar predication is also obtained for the graphane and silicane nanoribbons[40]. It is noted that the

monotonous reduction in bandgap is a desired property since these nanostructures could offer controllable band gap, which is crucial for nanoelectronic applications. We further have fitted the discrete band-gap values on the basis of exponential decay function:

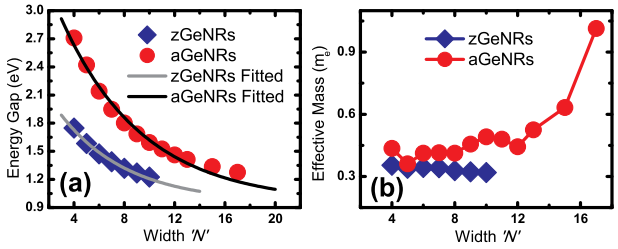

Fig. 9 (Color Online) Calculated (a) electronic band gaps and (b) electron effective mass as a function of ribbon width N for zGeNRs and aGeNRs.

$$E_{gap}(N) = 0.95eV + \lambda exp(-N\nu) \quad (7)$$

The fitted parameters λ and ν are 1.629 eV and 0.186 for the zGeNRs, and 3.116 eV and 0.154 for the aGeNRs, respectively. The electronic band gaps of both types of GeNRs reach $0.95eV$ as $N \to \infty$. According to the fitted curve, the modulation of band gap is moderate as $N < 12$ for zGeNRs and $N < 20$ for aGeNRs. Hence, the band gaps of the GeNRs have exhibited the same quantitative trends regardless of their edge shapes. Except for the variations in band gaps due to the shift of VBM and CBM, width N dependence of the electronic band structures of the GeNRs is found to be very small. On the other hand, similar to the bandgap engineering of the 2D germanane sheet, previous calculations have shown that the bandgap of the GeNRs can be effectively reduced by tensile strains[51,62]. The obtained width-dependent bandgap for the GeNRs are shown to be consistence with recent survey[35], thus the GeNRs with width-insensitive bandgap could be preferable for nanodevice applications.

The electron transport properties are determined not only by the bandgap scale, but also by the dispersion character associated with electron effective mass (m^*). The major differences observed in the electronic bands between the zGeNRs and aGeNRs are the different dispersion characteristics at the CBM subband. The m^* of the CBM for both zGeNRs and aGeNRs are presented in Figure 8b, which are calculated from the above $E(k)$ relationship by using the formula:

$$m^* = \hbar^2 (\frac{\partial^2 E(k)}{\partial k^2})^{-1} \quad (8)$$

The calculated m^* of the zGeNRs are systemically smaller than those of the aGeNRs. As a result, the electron transport in zGeNRs is expected to prior to the aGeNRs. In general, the m^* in zGeNRs proportionally decrease with width N increasing. In sharp contrast to the decreasing tread in zGeNRs, the aGeNRs exhibited nonmonotonic fashion and increasing tread in the effective mass, which is due to the dispersionless feature for the subband near the X point. Based on the analysis of m^* mentioned above, the zGeNRs and aGeNRs of the same width are predicted to present distinct transport properties, in spite they have very close band gaps.

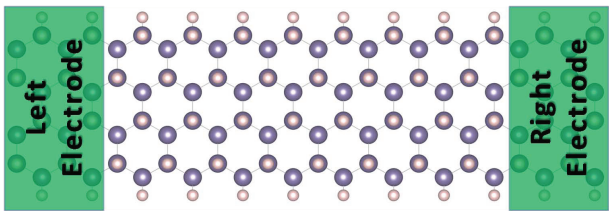

Fig. 10 (Color Online) Schematic of two-probe system of the 4-zGeNR nanodevice. The central region and the two electrodes are composed of pristine GeNRs.

To quantitatively evaluate the electron transport properties of the GeNRs, we have built the two-probe system nanodevice consisting of central region sandwiched by the left- and the right-electrode, which is schematically illustrated in Figure 10. The central region and the two electrodes are composed of the pristine GeNRs. Because of GeNRs presenting NM ground state, we choose 2 unit cell (1 unit cell) NM GeNR as electrodes that seamlessly connected with the central region comprising of 8 unit cell (5 unit cell) NM GeNR along electron transport direction for the zigzag- (armchair-) case. The quantum conductances $G = TG_0$ ($G_0 = 2e^2/h$ is the quantum conductance unit and T is the transmission coefficient) for the 4-zGeNR (1.468 nm in width) and 7-aGeNR (1.475 nm in width) are calculated for comparisons and are shown in Figure 11. The ballistic conductance gaps for the 4-zGeNR and 7-aGeNR are $1.64eV$ and $1.84eV$, respectively. These conductance gap values are in consistence with their electronic band gaps. The ballistic transport through one channel ($G = 1G_0$ for the quantum conductance) can be opened by a large external electric field ($\sim 1.8V$). Note that the quantum conductance of the 4-zGeNR is larger than that of the 7-aGeNR because more transmission channels are available in the former, while both present similar electronic band structures. The quantum conductance feature described above indicated that the electron transport could be more pronounced in the zGeNRs. Indeed, as shown in Figure 12 for the cases of the 4-zGeNR and the 7-aGeNR, the $I - V_b$ curve has revealed different transport behaviors depending on the GeNRs' edge topology, i.e., the electric conductivity $\sigma = 4396.50nS$ for the 4-aGeNR in comparison to $\sigma = 735.09nS$ for the 7-aGeNR (estimated from the calculated $I - V_b$ curve by equation $\sigma = \frac{\Delta I}{\Delta V}$). This is reminiscent of distinct differences in effective mass already ana-

lyzed. It also suggests that the transport properties in 2D germanane sheet are strongly anisotropic, leading to directional dependence of electron transport, which is in good agreement with previous theoretical study[36]. Hence, the calculated results have shown the possibility of controlling the $I-V_b$ performance by engineering the 2D germanane nanostructure to form zigzag- or armchair-edged morphology.

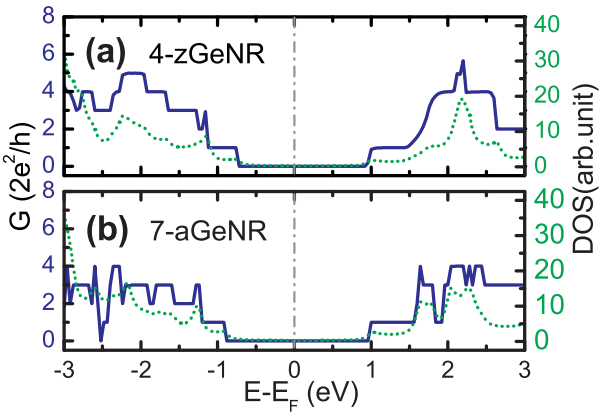

Fig. 11 (Color Online) Conductance (solid navy line) and DOS (dotted green line) as a function of electron energy for the 4-zGeNR (top panel) and the 7-aGeNR (bottom panel).

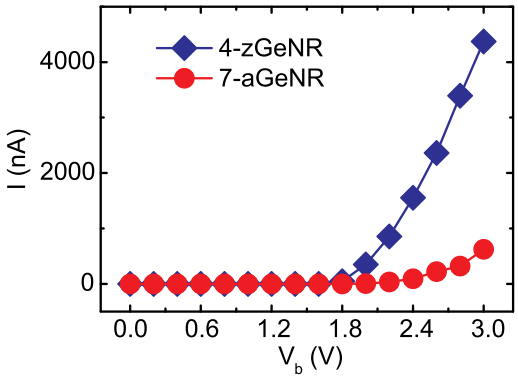

Fig. 12 (Color Online) The $I-V_b$ curve of the 4-zGeNR and 7-aGeNR.

3.5 Dehydrogenation in Germanane Ribbons

As in the case of 2D germanane sheet comprising of single H vacancy, the H monovacancy located at the center of the 13-aGeNR also induces magnetization by $1\mu_B$. It has been shown that both one-sided and two-sided H vacancy clusters can make 2D germanane sheet obtain magnetism[53,63]. Since

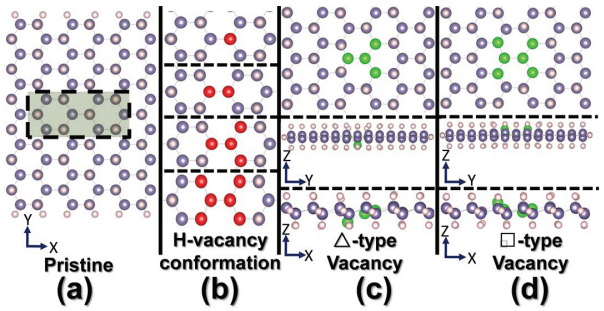

Fig. 13 (Color Online) The atomic conformations of the dehydrogenated 13-aGeNRs. Purple (dark) and white (light) represent Ge and H atoms, and red corresponds to the Ge atoms with dehydrogenation. (a) is the pristine aGeNRs, and dashed black rectangle denotes the dehydrogenated area consisting of different H-vacancy conformations that will be further considered in (b). (b) From top to bottom panels are the single H monovacancy, line-type divacancy, Δ-type vacancy cluster, and □-type vacancy cluster conformations, respectively. Note that only a small part which includes vacancy region and its nearby atoms is shown. (c) and (d) are the optimized Δ-type and □-type vacancy conformations comprising top view and side views (from top to bottom panels), respectively. The defected Ge atoms with H dehydrogenation are highlighted by green color.

it is reported that double-sided H-vacancy cluster could give large magnetic moments in graphane nanoribbon[39], it is fairly interesting to examine possible magnetic properties in the GeNRs. In this content, we consider four different conformations of the two-sided H-vacancy defects in the 13-aGeNR. In particular, the Δ triangular- and □ rectangular-types can be created by removing four and six H atoms, respectively, as shown in Figure 13. Generally, based on the Liebs theorem[64], the net magnetic moment of the desorbed nanostructures can be roughly evaluated from the difference between the number of the two interpenetrating A- and B-sublattices, i.e. $\mu_{tot}=|m-n|\mu_B$, where m (n) is the number of H atoms removed from A-sublattice (B-sublattice) Ge atoms. Indeed, our calculated value of magnetic moments for the line-type divacancy confirmation is zero, which is in agreement with Liebs theorem. For the Δ-type conformation, however, our computational simulation has conducted a nonmagnetic moment, which is different to the case in graphane nanoribbons[39]. It is noticed that the atomic structures extensively rearrange via Jahn-Teller-type distortion in the lattice after the introduction of Δ- and □-types of vacancy conformation. For the defect region, as a matter of fact, the buckling feature is fundamentally broken and the dehydrogenated Ge atoms prefer ramp-like configuration, which is visualized in the bottom panel of Figure 13c-d. As a result, the interpenetrating A- and B-sublattices are not maintained for the defect region after atomic reconstruction. In this context, the nonmagnetic feature for

the Δ- and □-types is attributed to the extensive reconstruction in the atomic structures that leading to the absence of interpenetrating sublattices for the desorbed system. Our calculated results suggest that it is unlikely to achieve stable magnetic state in germanane via controlling the shape of the two-sided H-vacancy cluster, because the dehydrogenated nanostructures prefer breaking sublattices with nonmagnetic characteristics after atomic reconstruction. Compare to the dehydrogenation of germanane material, the chemical functionalization of germanane is expected to be a more promising route to modulate the magnetic state of germanane-based nanomaterial for spintronic applications[26]. Nevertheless, our electronic structure and transport calculations have demonstrated that the germanane nanostructure has both suitable quantum conductance gap and directionally dependent transport properties, making it an excellent candidate for nanoelectronic applications.

4 Conclusion

In summary, we have carried out first principles calculations combined with non-equilibrium Green's function to study the structural, spin-dependent electronic structure and transport properties of the germanane-based nanostructures. The presence of single hydrogen vacancy gives rise to magnetic properties to the nonmagnetic pristine germanane owing to the spontaneous magnetization. However, the dumbbell structure induced by Ge adatom attains nonmagnetic properties due to the suppression of spontaneous ferromagnetism transition, because the exchange energy is smaller than the cost in band energy. The pristine germanane sheet possesses significant light absorption at the infrared and ultraviolet-visible region of solar spectrum, paving the way for innovative optoelectronic applications. The estimated defect concentration in the germanane is very low at room temperature. Using *ab initio* MD simulation, we found that both H-monovacancy and dumbbell contained defective germanane nanostructures are thermally stable at room temperature; and they have redshift and blueshift of the light adsorption peak compared to that in the pristine germanene sheet, respectively. Both zGeNRs and aGeNRs are found to be NM semiconductors with direct band gap at the Γ-point, and their band gaps are monotonously decreased with increasing ribbon width. The electron effective masses of the zGeNRs are systematically smaller than those of the aGeNRs. The quantum transport calculations have demonstrated different transport behaviors depending on the GeNRs' edge topology. The aGeNRs attain magnetic moment by means of creating H monovacancy at their surfaces. However, for the △-type conformation, our computational simulation revealed it is a nonmagnetic semiconductor, which is different to the case in graphane nanoribbons. This is originated from the extensive reconstruction in the atomic structures that leading to the absence of interpenetrating sublattices for the desorbed system. It suggest that the chemical functionalization of germanane could be a more promising route to modulate the magnetic state of germanane-based nanomaterial for spintronic applications. Hence, our calculated results have shown that the germanane-based nanomaterials have suitable conductance gap, light adsorption, and directionally dependent electron transport, making them excellent candidates for nanoelectronic and optoelectronic applications.

5 Acknowledgements

We are grateful to Prof. B.-G. Wang for providing code to perform the quantum transport calculations, and Prof. H.-J. Zhang for electronic structure simulations. The authors would like to thank Dr. Y.-H. Zhao for technical assistance on performing partial calculations in the HPCC@SICNU, and Dr. J.-W. Wei for useful and inspirational discussions. This work is financially supported by Natural Science Foundation of China (Grant Nos. 11304022, 11347010, 11404037, and 11204391), and China Postdoctoral Science Foundation (Grant No. 2015M571729).

References

1 K. S. Novoselov, A. K. Geim, S. V. Morozov, D. Jiang, Y. Zhang, S. V. Dubonos, I. V. Grigorieva and A. A. Firsov, *Science*, 2004, **306**, 606–609.
2 K. S. Novoselov, V. I. Falko, L. Colombo, P. R. Gellert, M. G. Schwab and K. Kim, *Nature*, 2012, **490**, 192–200.
3 P. Avouris and C. Dimitrakopoulos, *Mater. Today*, 2012, **15**, 86–97.
4 A. K. Geim and I. V. Grigorieva, *Nature*, 2013, **339**, 419–425.
5 C. Y. Zhi, Y. Bando, C. C. Tang, H. Kuwahara and D. Golberg, *Adv. Mater.*, 2009, **21**, 2889–2893.
6 B. Yan and S. C. Zhang, *Rep. Prog. Phys.*, 2012, **75**, 096501.
7 M. Chhowalla, H. S. Shin, G. Eda, L.-J. Li, K. P. Loh and H. Zhang, *Nat. Chem.*, 2013, **5**, 263–275.
8 M. Xu, T. Liang, M. Shi and H. Chen, *Chem. Rev.*, 2013, **113**, 3766–3798.
9 K. F. Mak, C. Lee, J. Hone, J. Shan and T. F. Heinz, *Phys. Rev. Lett.*, 2010, **105**, 136805.
10 S. Cahangirov, M. Topsakal, E. Aktürk, H. Şahin and S. Ciraci, *Phys. Rev. Lett.*, 2009, **102**, 236804.
11 M. Houssa, E. Scalise, K. Sankaran, G. Pourtois, V. V. Afanasev and A. Stesmans, *Appl. Phys. Lett.*, 2011, **98**, 223107.
12 J. C. Garcia, D. B. de Lima, L. V. C. Assali and J. F. Justo, *J Phys. Chem. C*, 2011, **115**, 13242–13246.
13 Y. Xu, B. Yan, H.-J. Zhang, J. Wang, G. Xu, P. Tang, W. Duan and S.-C. Zhang, *Phys. Rev. Lett.*, 2013, **111**, 136804.
14 Q. Tang and Z. Zhou, *Prog. Mater. Sci.*, 2013, **58**, 1244–1315.
15 S. Balendhran, S. Walia, H. Nili, S. Sriram and M. Bhaskaran, *Small*, 2015, **11**, 640–652.
16 P. Vogt, P. D. Padova, C. Quaresima, J. Avila, E. Frantzeskakis, M. C. Asensio, A. Resta, B. Ealet and G. L. Lay, *Phys. Rev. Lett.*, 2012, **108**, 155501.
17 B. J. Feng, Z. Ding, S. Meng, Y. Yao, X. He, P. Cheng, L. Chen and K. Wu, *Nano Lett.*, 2012, **12**, 3507–3511.
18 A. Fleurence, R. Friedlein, T. Ozaki, H. Kawai, Y. Wang and Y. Yamada-Takamura, *Phys. Rev. Lett.*, 2012, **108**, 245501.

19 M. Satta, S. Colonna, R. Flammini, A. Cricenti and F. Ronci, *Phys. Rev. Lett.*, 2015, **115**, 026102.
20 M. E. Dávila, L. Xian, S. Cahangirov, A. Rubio and G. L. Lay, *New J. Phys.*, 2014, **16**, 095002.
21 F.-F. Zhu, W.-J. Chen, Y. Xu, C.-L. Gao, D.-D. Guan, C.-H. Liu, D. Qian, S.-C. Zhang and J.-F. Jia, *Nat. Mater.*, 2015, **14**, 1020–1025.
22 E. Bianco, S. Butler, S. Jiang, O. D. Restrepo, W. Windl and J. E. Goldberger, *ACS Nano*, 2013, **7**, 4414–4421.
23 S. Jiang, E. Biancoa and J. E. Goldberger, *J. Mater. Chem. C*, 2014, **2**, 3185–3188.
24 O. D. Restrepo, K. E. Krymowski, J. Goldberger and W. Windl, *New J. Phys.*, 2014, **16**, 105009.
25 S. Z. Butler, S. M. Hollen, L. Cao, Y. Cui, J. A. Gupta, H. R. Gutirrez, T. F. Heinz, S. S. Hong, J. Huang, A. F. Ismach, E. Johnston-Halperin, M. Kuno, V. V. Plashnitsa, R. D. Robinson, R. S. Ruoff, S. Salahuddin, J. Shan, L. Shi, M. G. Spencer, M. Terrones, W. Windl and J. E. Goldberger, *ACS Nano*, 2013, **7**, 2898–2926.
26 S. Jiang, M. Q. Arguilla, N. D. Cultrara and J. E. Goldberger, *Acc. Chem. Res.*, 2015, **79**, 144–151.
27 Q. Tang, Z. Zhou and Z. Chen, *WIREs Comput. Mol. Sci.*, 2015, **5**, 360–379.
28 S. Jiang, S. Butler, E. Bianco, O. D. Restrepo, W. Windl and J. E. Goldberger, *Nat. Commun.*, 2014, **5**, 3389.
29 I. V. Pinchuk, P. M. Odenthal, A. S. Ahmed, W. Amamou, J. E. Goldberger and R. K. Kawakami, *J. Mater. Res.*, 2014, **29**, 410–416.
30 W. Amamou, P. M. Odenthal, E. J. Bushong, D. J. ÓHara, Y. K. Luo, J. van Baren, I. Pinchuk, Y. Wu, A. S. Ahmed, J. Katoch, M. W. Bockrath, H. W. K. Tom, J. E. Goldberger and R. K. Kawakami, *2D Materials*, 2015, **2**, 035012.
31 L. C. L. Y. Voon, E. Sandberg, R. S. Aga and A. A. Farajian, *Appl. Phys. Lett.*, 2010, **97**, 163114.
32 O. Pulci, P. Gori, M. Marsili, V. Garbuio, R. D. Sole and F. Bechstedt, *Europhys. Lett.*, 2012, **98**, 37004.
33 W. Wei, Y. Dai, B. Huang and T. Jacob, *Phys. Chem. Chem. Phys.*, 2013, **15**, 8789–8794.
34 F. Matusalem, M. Marques, L. K. Teles and F. Bechstedt, *Phys. Rev. B*, 2015, **92**, 045436.
35 Y. Zhou, X. Li, Z. Wang, S. Li and X. Zu, *Phys. Chem. Chem. Phys.*, 2014, **16**, 18029–18033.
36 R. K. Ghosh, M. Brahma and S. Mahapatra, *IEEE T. Electron Dev.*, 2014, **61**, 2309–2315.
37 K. L. Low, W. Huang, Y.-C. Yeo and G. Liang, *IEEE T. Electron Dev.*, 2014, **61**, 1590–1598.
38 Q. Tang, Z. Zhou and Z. Chen, *Nanoscale*, 2013, **5**, 4541–4583.
39 H. Sahin, C. Ataca and S. Ciraci, *Phys. Rev. B*, 2010, **81**, 205417.
40 J. Kim and M. V. Fischetti, *Phys. Rev. B*, 2012, **86**, 205323.
41 G. Kresse and J. Furthmuller, *Phys. Rev. B*, 1996, **54**, 11169–11186.
42 J. P. Perdew, K. Burke and M. Ernzerhof, *Phys. Rev. Lett.*, 1996, **77**, 3865–3868.
43 H. J. Monkhorst and J. D. Pack, *Phys. Rev. B*, 1976, **13**, 5188–5192.
44 J. Taylor, H. Guo and J. Wang, *Phys. Rev. B*, 2001, **63**, 245407.
45 M. Brandbyge, J. L. Mozos, P. Ordejón, J. Taylor and K. Stokbro, *Phys. Rev. B*, 2002, **65**, 165401.
46 N. Toullier and J. L. Martins, *Phys. Rev. B*, 1991, **43**, 1993–2006.
47 M. Büttiker, *Phys. Rev. Lett.*, 1986, **57**, 1761–1764.
48 S. Datta, *Quantum Transport: Atom to Transistor*, Cambridge University Press, New York, U.S.A., 1st edn, 2005.
49 K. Momma and F. Izumi, *J. Appl. Cryst.*, 2011, **44**, 1272–1276.
50 C. Si, J. Liu, Y. Xu, J. Wu, B.-L. Gu and W. Duan, *Phys. Rev. B*, 2014, **89**, 115429.
51 Y. Li and Z. Chen, *J . Phys. Chem. C*, 2014, **118**, 1148–1154.
52 Q. Pang, Y. Zhang, J.-M. Zhang, V. Ji and K.-W. Xu, *Nanoscale*, 2011, **3**, 4330–4338.
53 Y. Zhou, K. Liu, H. Xiao, X. Xiang, J. Nie, S. Li, H. Huang and X. Zu, *J. Mater. Chem. C*, 2015, **3**, 3128–3134.
54 C. Kittel, *Introduction to Solid State Physics*, John Wiley and Sons, Inc, New York, U.S.A., 8th edn, 2005.
55 V. O. Özçelik and S. Ciraci, *J. Phys. Chem. C*, 2013, **117**, 26305–26315.
56 J. Gao, J. Zhang, H. Liu, Q. Zhang and J. Zhao, *Nanoscale*, 2013, **5**, 9785–9792.
57 E. Kaxiras, *Atomic and Electronic Structure of Solids*, Cambridge University Press, New York, U.S.A., 1st edn, 2003.
58 Q. Pang, L. Li, L.-L. Zhang, C.-L. Zhang and Y.-L. Song, *Can. J. Phys.*, 2015, **93**, 1310–1318.
59 M. Gajdoš, K. Hummer, G. Kresse, J. Furthmüller and F. Bechstedt, *Phys. Rev. B*, 2006, **73**, 045112.
60 Y.-W. Son, M. L. Cohen and S. G. Louie, *Phys. Rev. Lett.*, 2006, **97**, 216803.
61 T. Wassmann, A. P. Seitsonen, A. M. Saitta, M. Lazzeri and F. Mauri, *Phys. Rev. Lett.*, 2008, **101**, 096402.
62 S. Dong and C.-Q. Chen, *J. Phys.: Condens. Matter*, 2015, **27**, 245303.
63 X.-Q. Wang, H.-D. Li and J.-T. Wang, *Phys. Chem. Chem. Phys.*, 2012, **14**, 3031–3036.
64 E. H. Lieb, *Phys. Rev. Lett.*, 1989, **62**, 1201–1204.